Electronic Supplementary Material (ESI) for Journal of Materials Chemistry A.

Cationic vacancies and interface engineering on crystalline-amorphous gamma-phase Ni-Co oxyhydroxides achieve ultrahigh mass/areal/volumetric energy density flexible all-solid-state asymmetric supercapacitor

Xue Ren,[†a] Menggang Li,[†a] Longyu Qiu,[†a] Xin Guo,[a] Fenyang Tian,[a] Guanghui Han,[a] Weiwei Yang*[a] and Yongsheng Yu*[a]

[a] State Key Laboratory of Urban Water Resource and Environment, School of Chemistry and Chemical Engineering, Harbin Institute of Technology, Harbin, Heilongjiang 150001, China.

* Corresponding authors.

E-mail: yangww@hit.edu.cn (W. Yang), ysyu@hit.edu.cn (Y. Yu).

[†] These authors contributed equally to the work.

Experimental Section

Materials: Nickel foam (Guangzhou Jiayuan New Material Technology Co., Ltd). Ethanol (C_2H_5OH), potassium hydroxide (KOH), polyvinyl alcohol (PVA), polytetrafluoroethylene (PTFE), sodium sulphide ($Na_2S{\cdot}9H_2O$), sodium hypophosphite hydrate ($NaH_2PO_2{\cdot}H_2O$), cobalt nitrate hexahydrate ($Co(NO_3)_2{\cdot}6H_2O$) and potassium chloride (KCl) were all purchased from Aladdin. All the chemicals are purchased commercially and used without further purification.

Characterizations: The morphology of as-prepared self-supporting electrode materials were taken by scanning electron microscopy (SEM) using a JEOL JSM-6360 (JEOL, Japan). The crystalline structure of as-obtained self-supporting electrode materials were analyzed by X-ray diffraction (XRD) patterns on a PAN analytical X'Pert Powder with Cu Kα radiation (λ = 1.5418 Å). Transmission electron microscopy (TEM) images were observed on Tecnai G2 F30 electron microscope (FEI Company, America). X-ray photoelectron spectroscopies (XPS) were obtained on a Thermo Scientific Escalab 250Xi (Thermo Fisher Scientific, America), and the binding energies in XPS analysis were corrected by referencing C 1s to 284.6 eV. *In-situ* Raman spectra were obtained using a Renishaw inVia reflex Raman microscope with an excitation wavelength of 532 nm in an electrochemical workstation (CHI 760E, ChenHua Corp., Shanghai, China) and the Raman spectroscopy electrolytic cell (K006, Tianjin Aida Hengsheng Technology Development Co., Ltd, Tianjin, China).

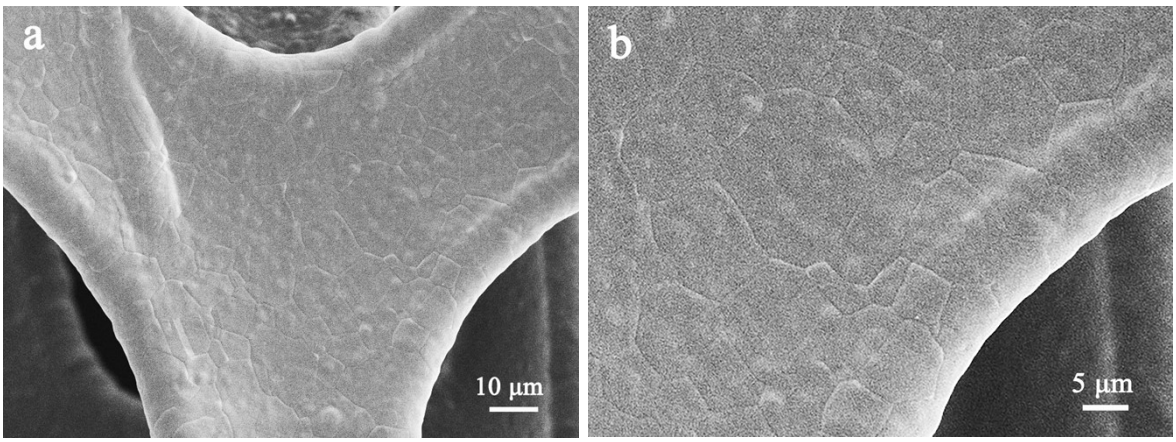

Figure S1. (a) Low- and (b) high-resolution SEM images of Ni foam.

The SEM images in **Figure S1** display that the bare Ni foam is full of Ni grain boundary network (the transverse size of about 5 to 20 μm). Ni foam is served as a satisfactory and cheap substrate, showing the advantages of superior conductivity, the higher specific surface area and structural stability.

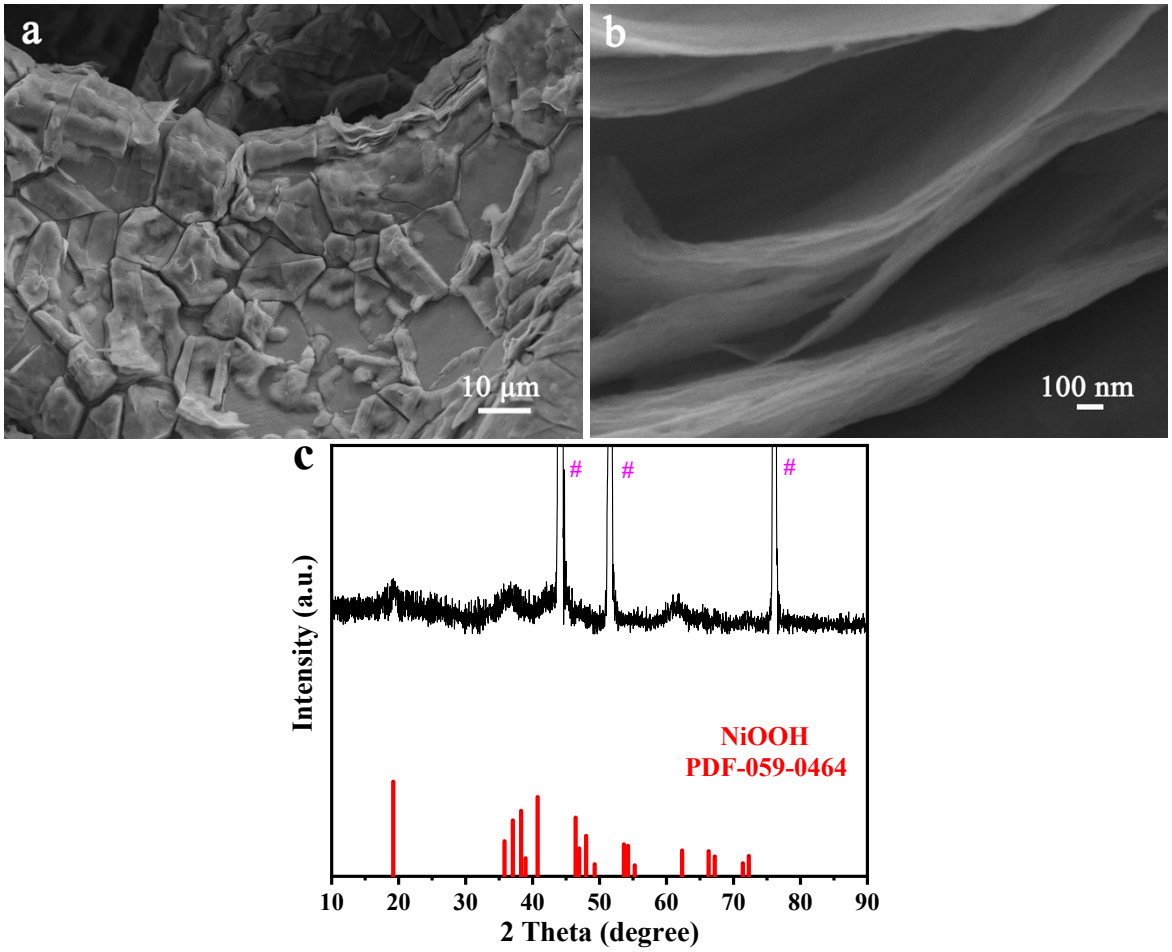

Figure S2. (a) Low-, (b) high-resolution SEM images and (c) XRD pattern of NiOOH (Ni peaks are marked with "#").

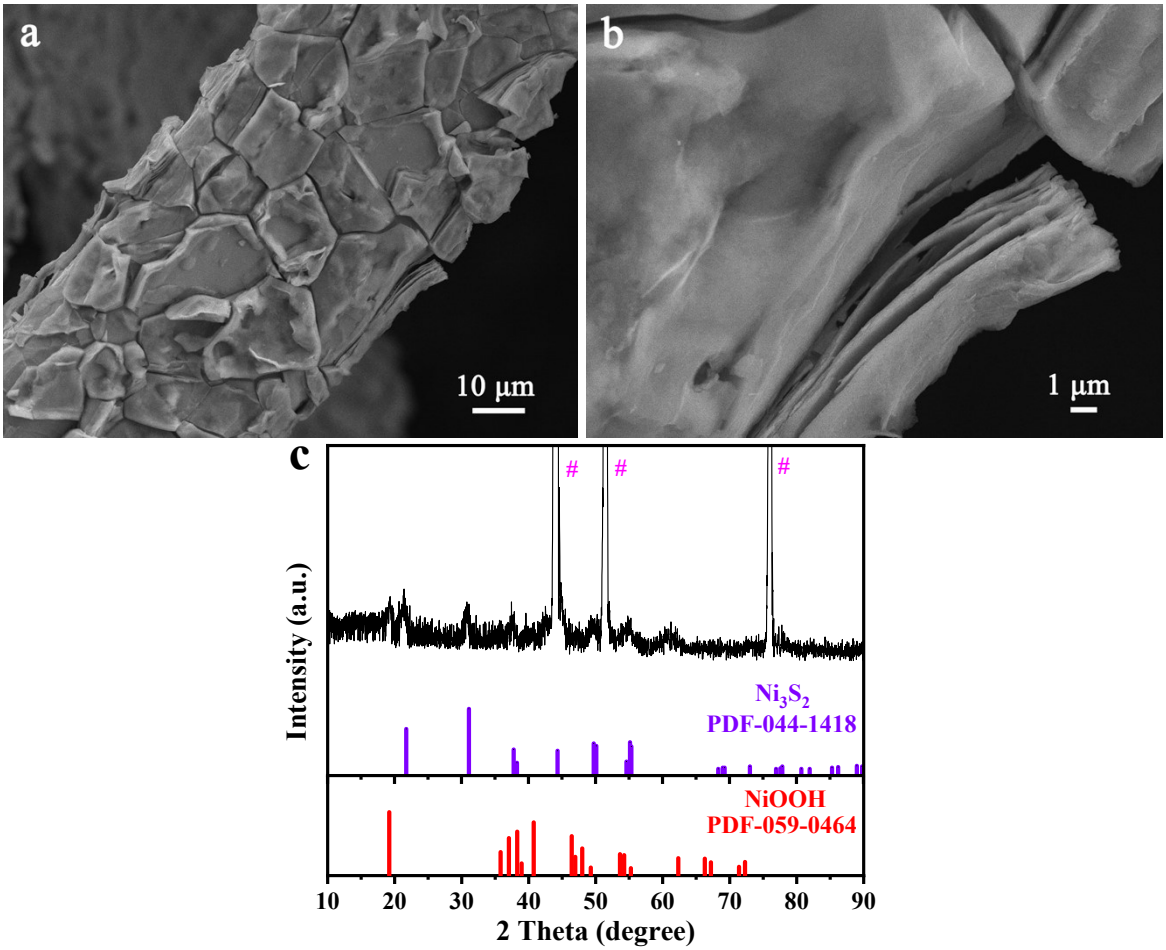

Figure S3. (a) Low-, (b) high-resolution SEM images and (c) XRD pattern of NiOOH@Ni_3S_2 (Ni peaks are marked with "#").

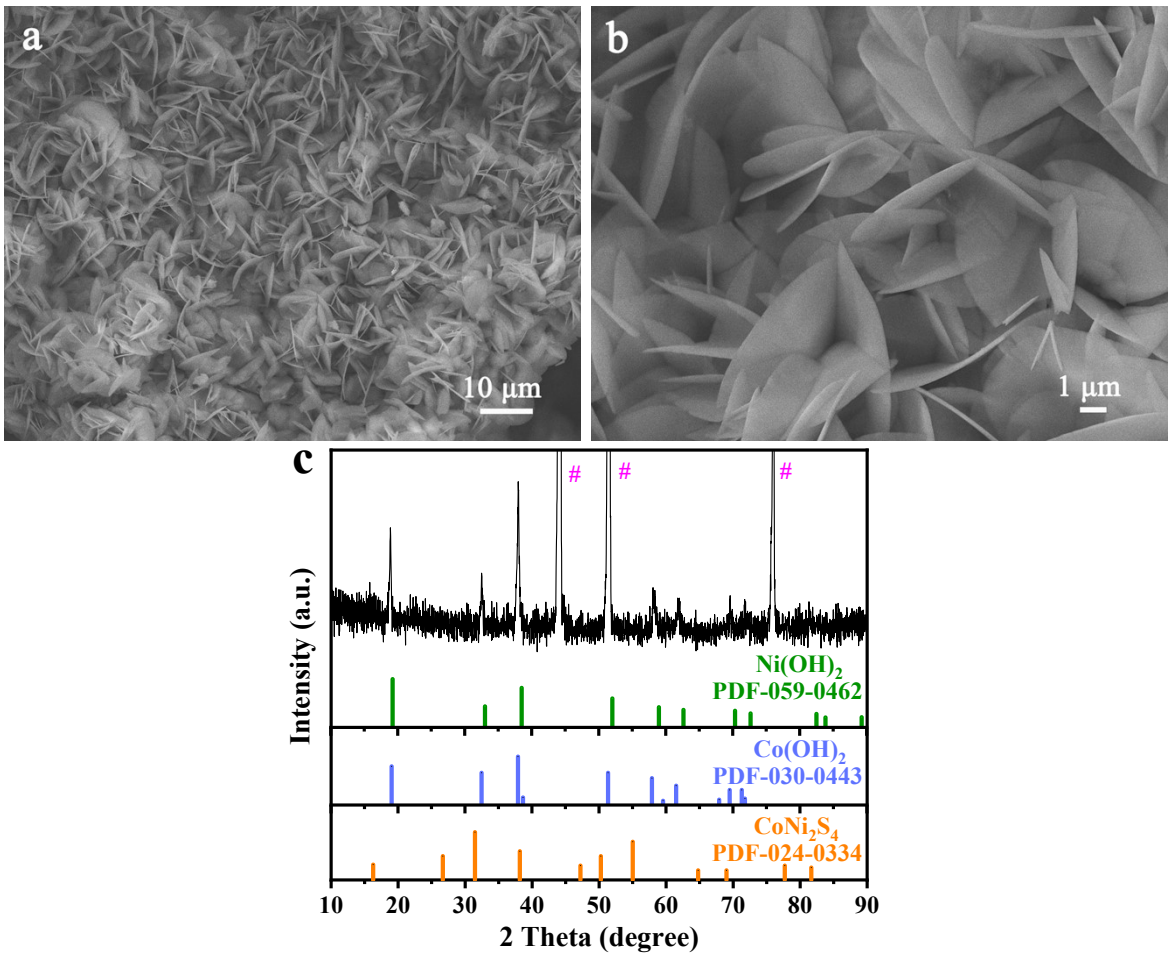

Figure S4. (a) Low-, (b) high-resolution SEM images and (c) XRD pattern of NiCo-LDH@$CoNi_2S_4$ (Ni peaks are marked with "#").

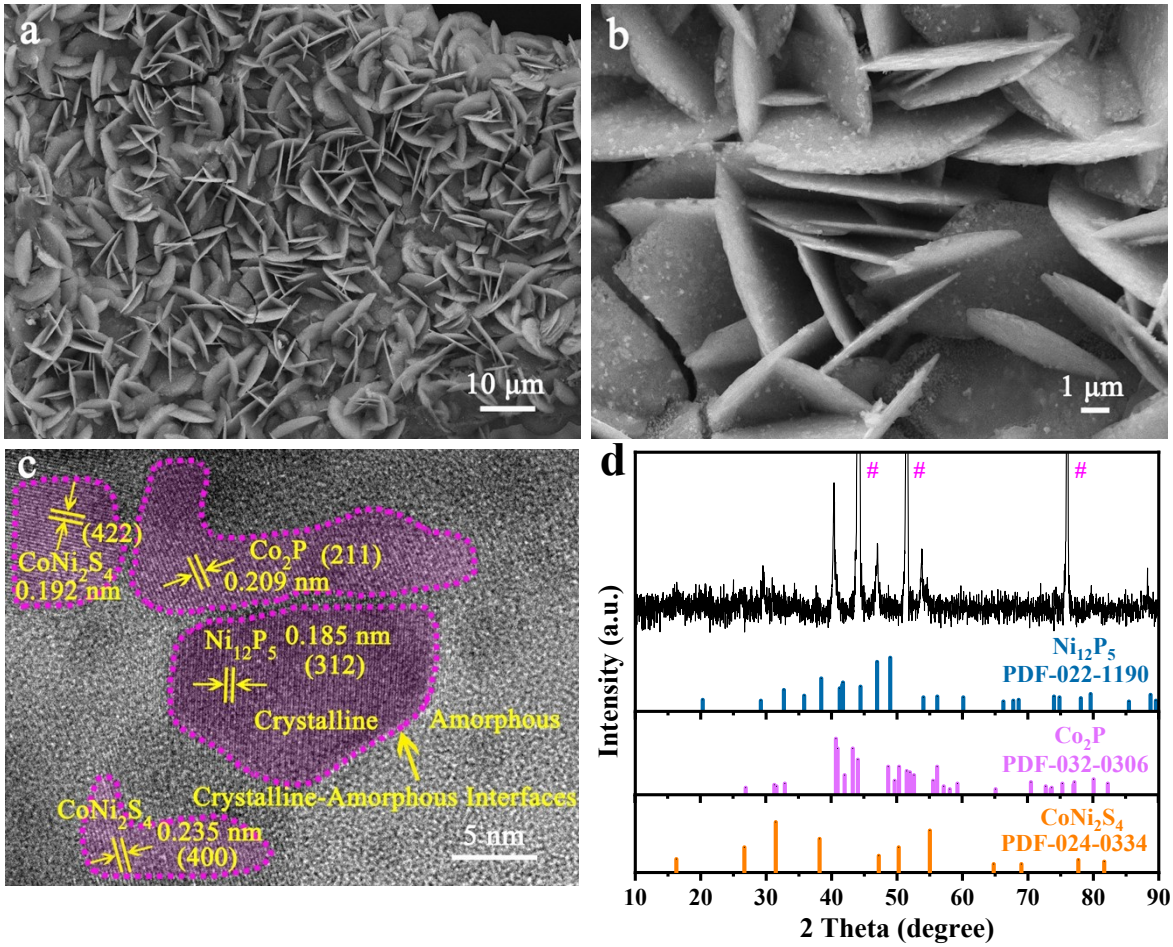

Figure S5. (a) Low-, (b) high-resolution SEM images, (c) HRTEM image and (d) XRD pattern of Ni-Co-P@$CoNi_2S_4$ (Ni peaks are marked with "#").

Compared with NiCo-LDH@$CoNi_2S_4$, the morphology change of Ni-Co-P@$CoNi_2S_4$ nanoplate is related to the anion-exchange reaction between NiCo-LDH@$CoNi_2S_4$ and P source under the assistance of heat treatment, resulting in the rough surface and volume expansion of Ni-Co-P@$CoNi_2S_4$ nanoplates.[1]

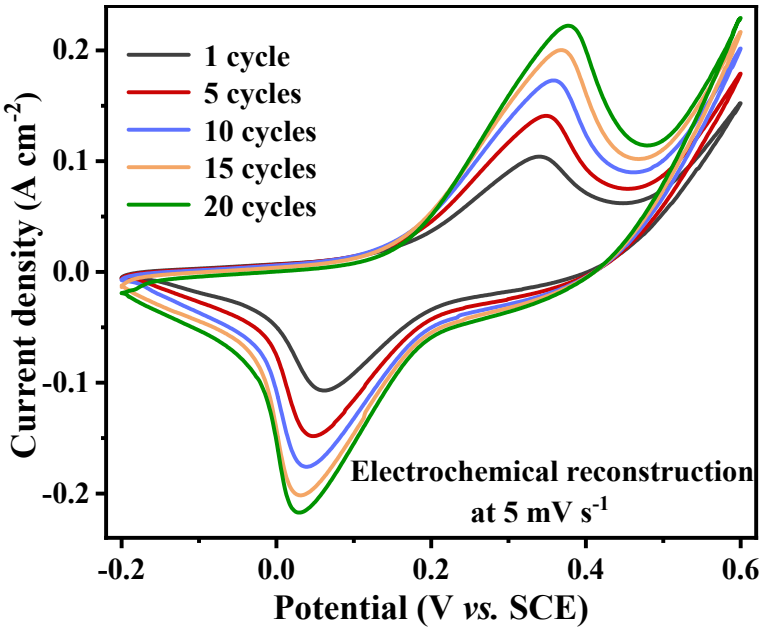

Figure S6. CV curves of Ni-Co oxyhydroxides for electrochemical reconstruction process collected at 5 mV s^{-1}.

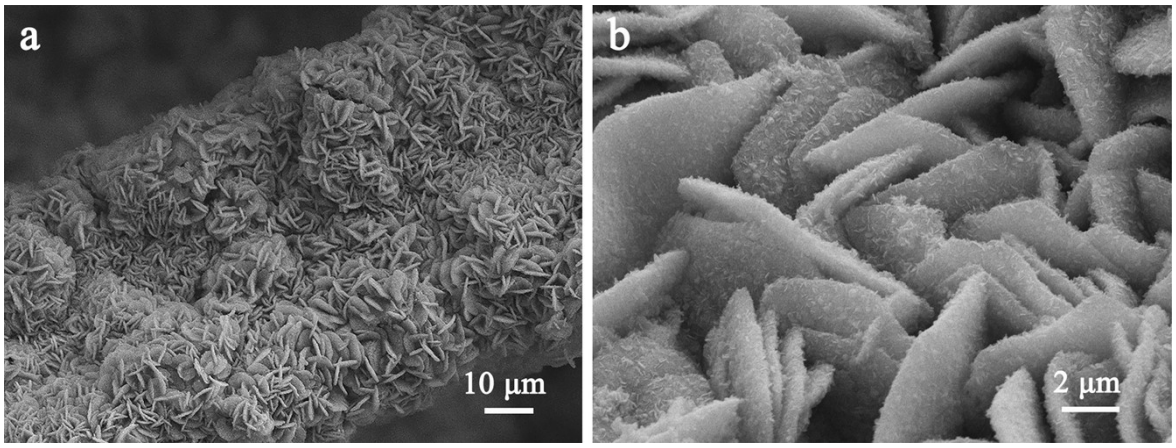

Figure S7. (a) Low-, and (b) high-resolution SEM images of Ni-Co oxyhydroxides.

The vertical cross-linking Ni-Co oxyhydroxides micron-scale nanoplates are uniformly distributed on the Ni substrate, which are composed of ultrathin hexagonal nano-scale nanosheets (**Figure S7**). This two-dimensional (2D) to three-dimensional (3D) hierarchical structure can provide abundant active sites, developed electrical percolative network, fast ion/electron transport path, high conductivity and excellent structural stability to achieve superior electrochemical performance for supercapacitors.

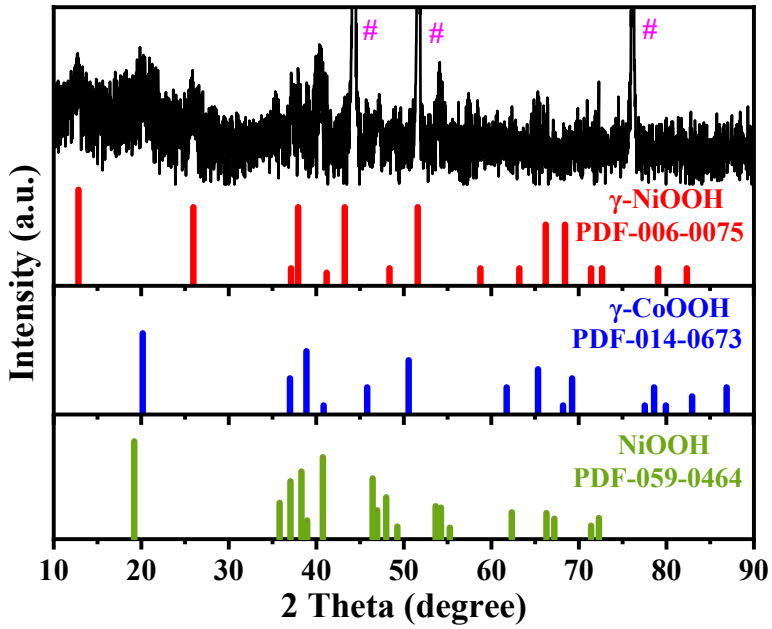

Figure S8. XRD pattern of Ni-Co oxyhydroxides (Ni peaks are marked with "#").

Figure S8 illustrates the XRD pattern of Ni-Co oxyhydroxides. Clearly, the intense diffraction peaks at 44.6°, 51.8° and 76.5° are assigned to the (111), (200) and (220) planes of Ni foam. The characteristic peaks at 12.7°, 25.9°, 37.8°, 43.1°, 51.1° and 66.1° indexed to the (003), (006), (102), (105), (108) and (110) planes of γ-NiOOH (PDF-006-0075), respectively, and the peaks at 20.2°, 37.1°, 38.6°, 45.9° and 65.5° correspond to the (003), (101), (012), (104) and (110) planes of the γ-CoOOH (PDF-014-0673), and the peaks at 19.3°, 35.6°, 40.8°, 46.4°, 53.9° and 62.4° correspond to the (002), (110), (112), (113), (114) and (205) planes of the NiOOH (PDF-059-0464), suggesting that the γ-phase Ni-Co oxyhydroxides have been successfully prepared on Ni foam *via* electrochemical reconstruction. Meanwhile, the weak diffraction peaks of Ni-Co oxyhydroxides further prove its crystalline-amorphous characteristics.

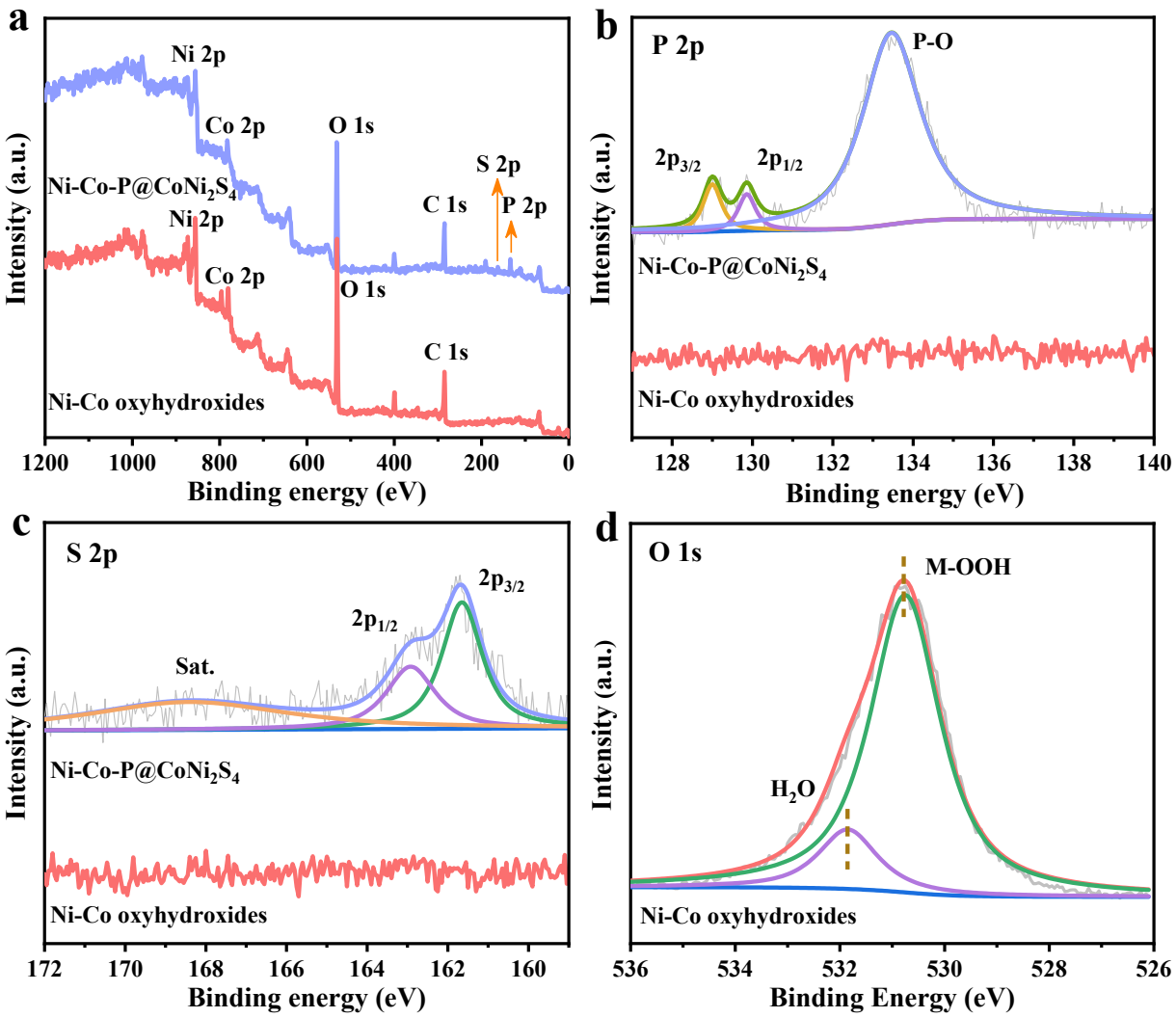

Figure S9. High-resolution XPS spectra of (a) survey spectra, (b) P 2p and (c) S 2p of the Ni-Co-P@$CoNi_2S_4$ and Ni-Co oxyhydroxides. (d) High-resolution O 1s XPS spectra of Ni-Co oxyhydroxides.

The C element is from the reference carbon or some unavoidable air contaminations, which also produces O signal. The peaks at 130 and 129.1 eV are assigned to P $2p_{1/2}$ and $2p_{3/2}$ of Ni-Co-P, and the peak at 133.5 eV is related to the inevitable oxidation of P during the storage, transportation and drying processes (**Figure S9b**). The peaks at 162.9 and 161.7 eV in XPS spectrum of Ni-Co-P@$CoNi_2S_4$ are corresponding to S $2p_{1/2}$ and S $2p_{3/2}$ (**Figure S9c**), the former ascribed to sulfur in low coordination and the latter related to the sulfur-metal bond, and the peak at 168.5 eV corresponds to sulfur in high oxidation states.[2] However, the P 2p and S 2p spectra for Ni-Co

oxyhydroxides with no detectable signals further explain that nearly all the P and S elements were leached from Ni-Co-P@$CoNi_2S_4$ after electrochemical reconstruction process. In addition, the peak at 530.7 eV for Ni-Co oxyhydroxides is corresponded to metal-oxyhydroxide (M-OOH), revealing the generation of O_2^{2-} species due to the formation of Ni-Co oxyhydroxides (**Figure S9d**). The peak at 531.9 eV for the O 1s XPS spectra of Ni-Co oxyhydroxides is attributed to physical/chemically absorpted water on the surface.[3]

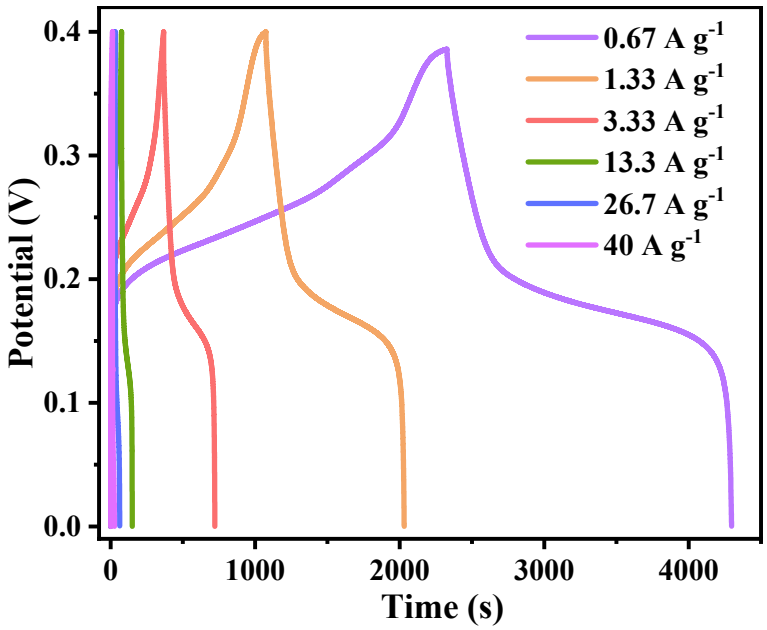

Figure S10. GCD curves of Ni-Co oxyhydroxides from 0.67 to 40 A g^{-1}.

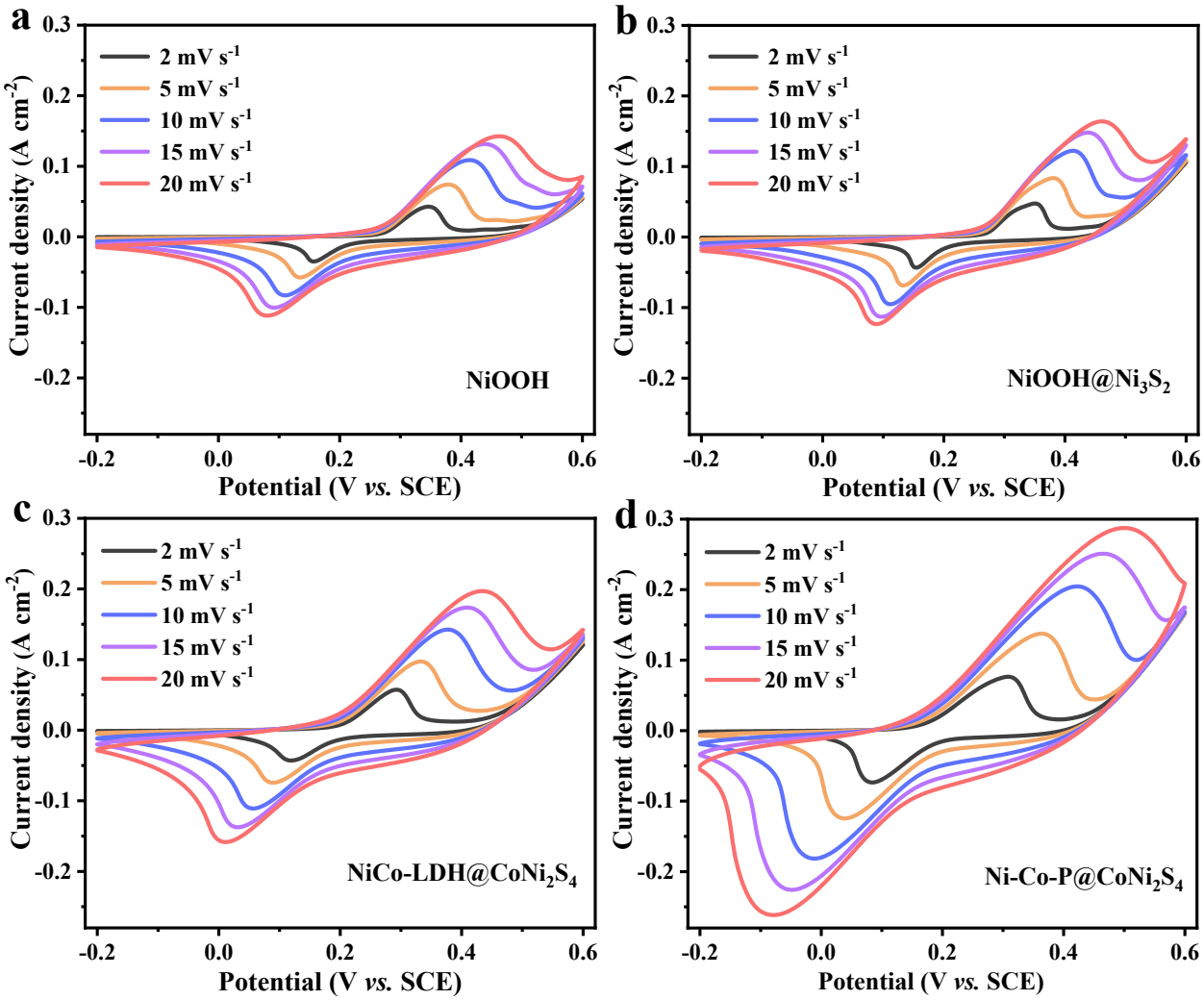

Figure S11. CV curves at different scan rates of (a) NiOOH, (b) NiOOH@Ni_3S_2, (c) NiCo-LDH@$CoNi_2S_4$ and (d) Ni-Co-P@$CoNi_2S_4$.

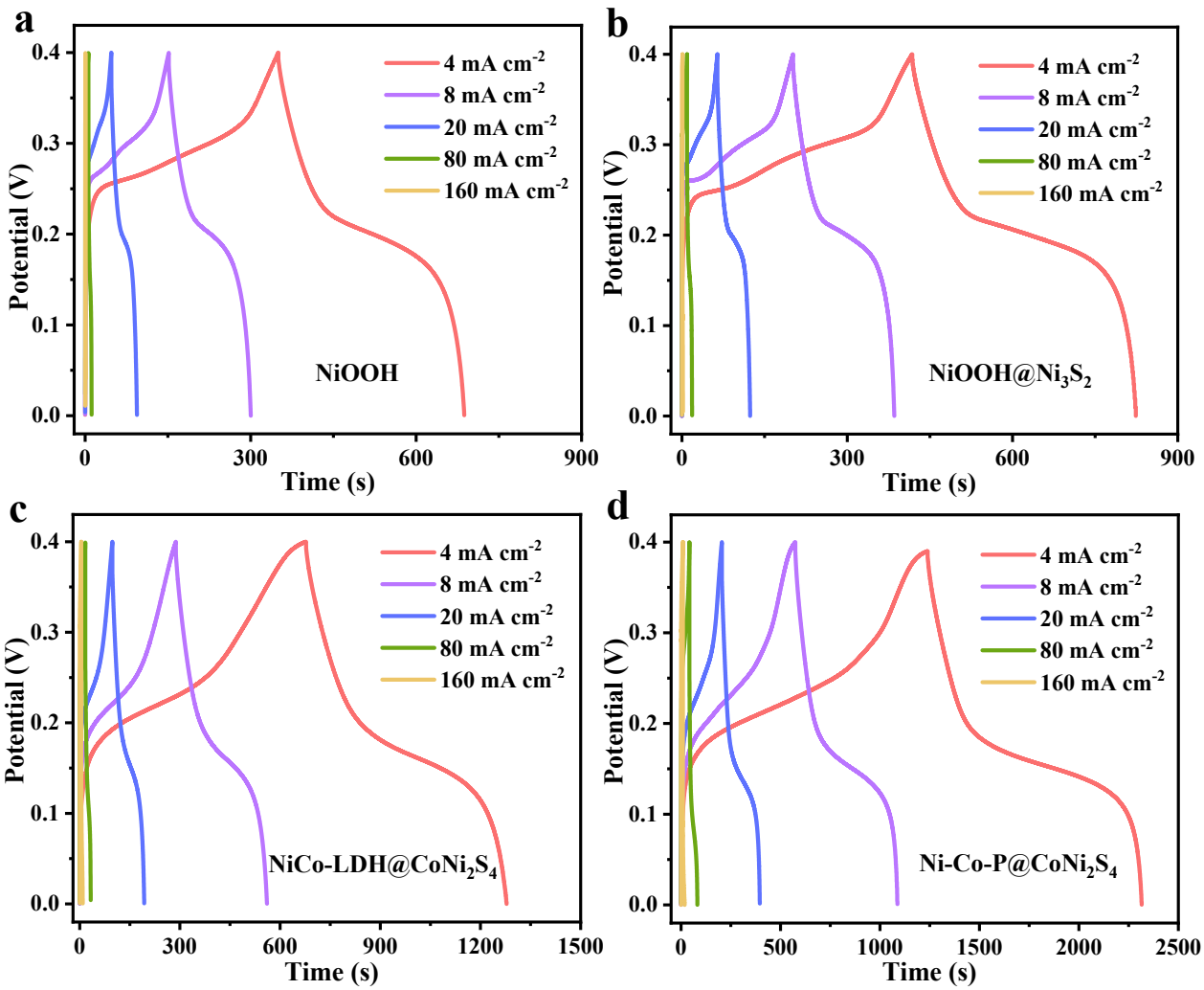

Figure S12. GCD curves of (a) NiOOH, (b) NiOOH@Ni_3S_2, (c) NiCo-LDH@$CoNi_2S_4$ and (d) Ni-Co-P@$CoNi_2S_4$ from 4 to 160 mA cm^{-2}.

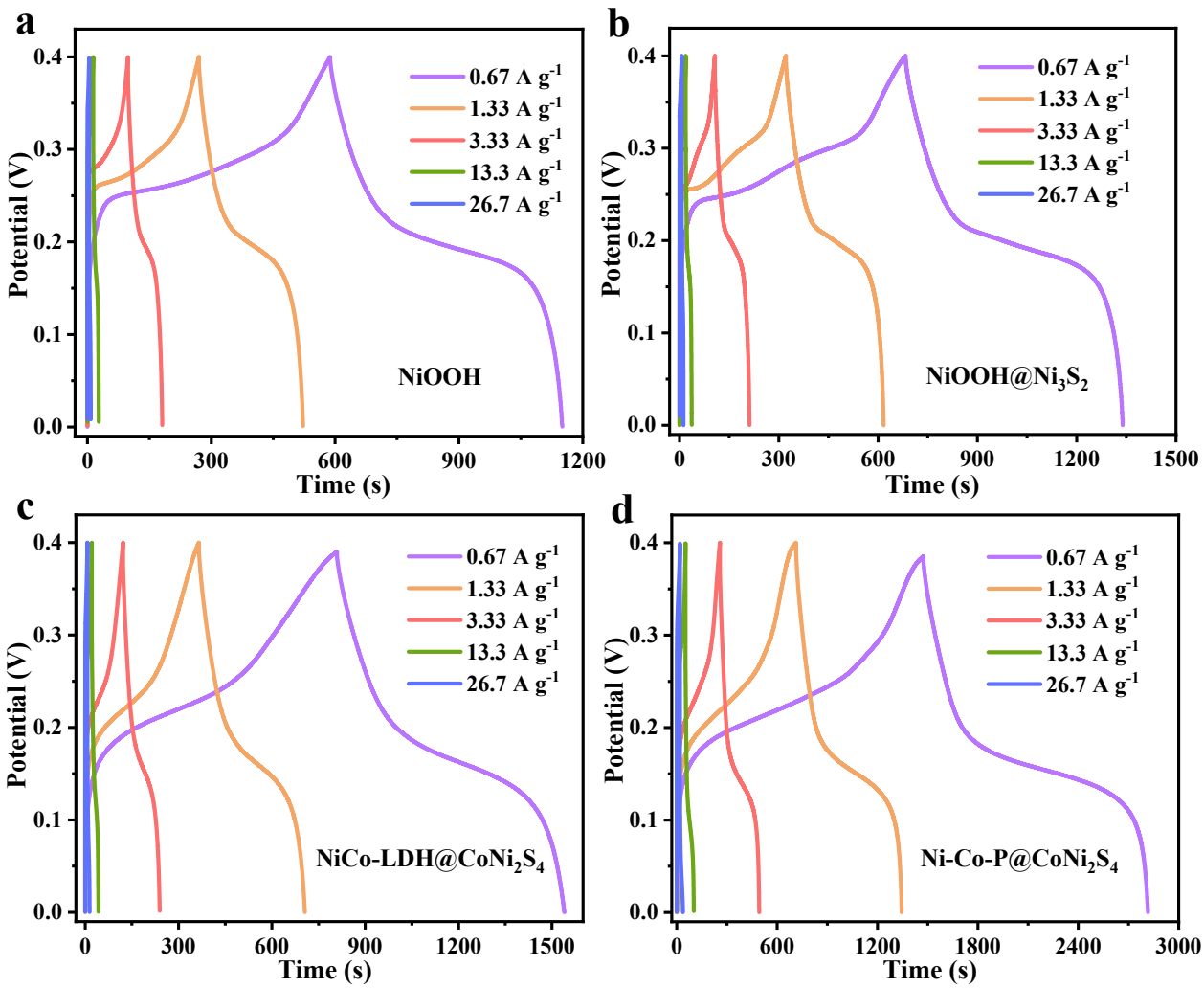

Figure S13. GCD curves of (a) NiOOH, (b) NiOOH@Ni_3S_2, (c) NiCo-LDH@$CoNi_2S_4$ and (d) Ni-Co-P@$CoNi_2S_4$ from 0.67 to 26.7 A g^{-1}.

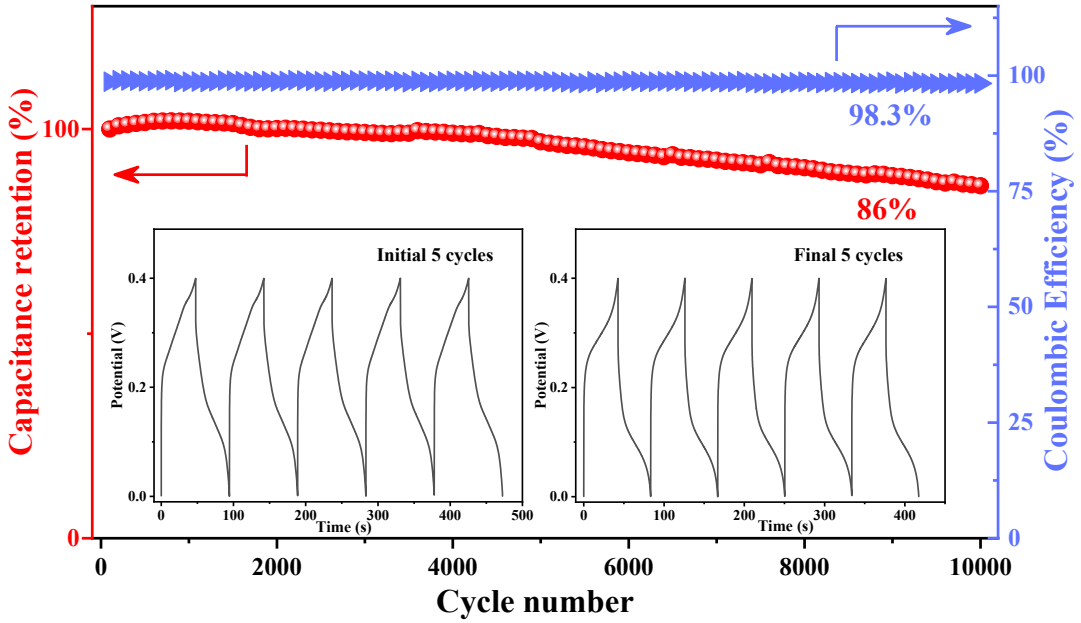

Figure S14. Cycling performance and coulombic efficiency of the Ni-Co oxyhydroxides (at 100 mA cm^{-2}) in three-electrode system.

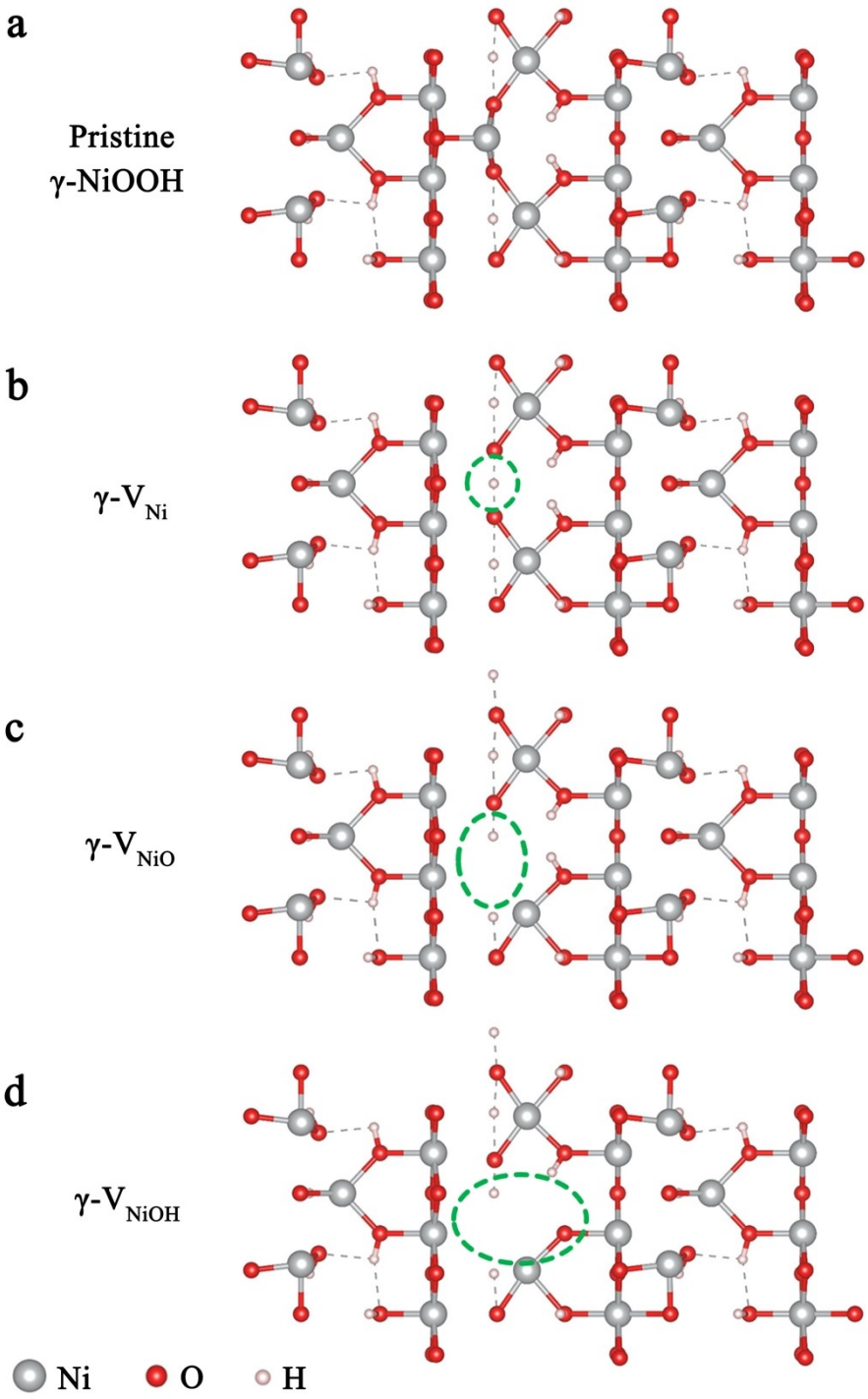

Figure S15. Top views of optimized geometries of pristine γ-NiOOH, γ-V_{Ni} (γ-NiOOH with Ni cation vacancy), γ-V_{NiO} (γ-NiOOH with NiO cation vacancy) and γ-V_{NiOH} (γ-NiOOH with NiOH cation vacancy).

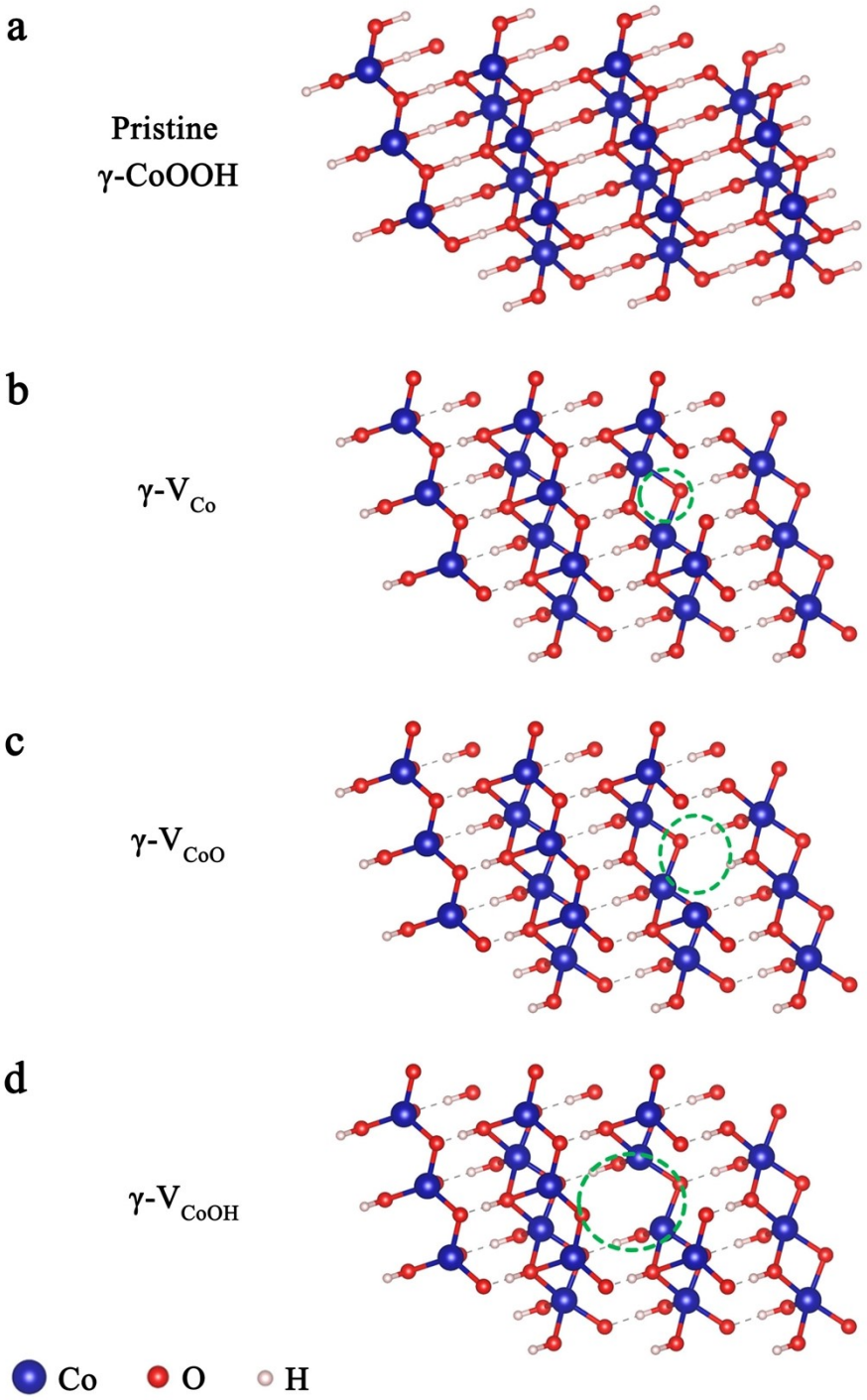

Figure S16. Top views of optimized geometries of pristine γ-CoOOH, γ-V_{Co} (γ-CoOOH with Co cation vacancy), γ-V_{CoO} (γ-CoOOH with CoO cation vacancy) and γ-V_{CoOH} (γ-CoOOH with CoOH cation vacancy).

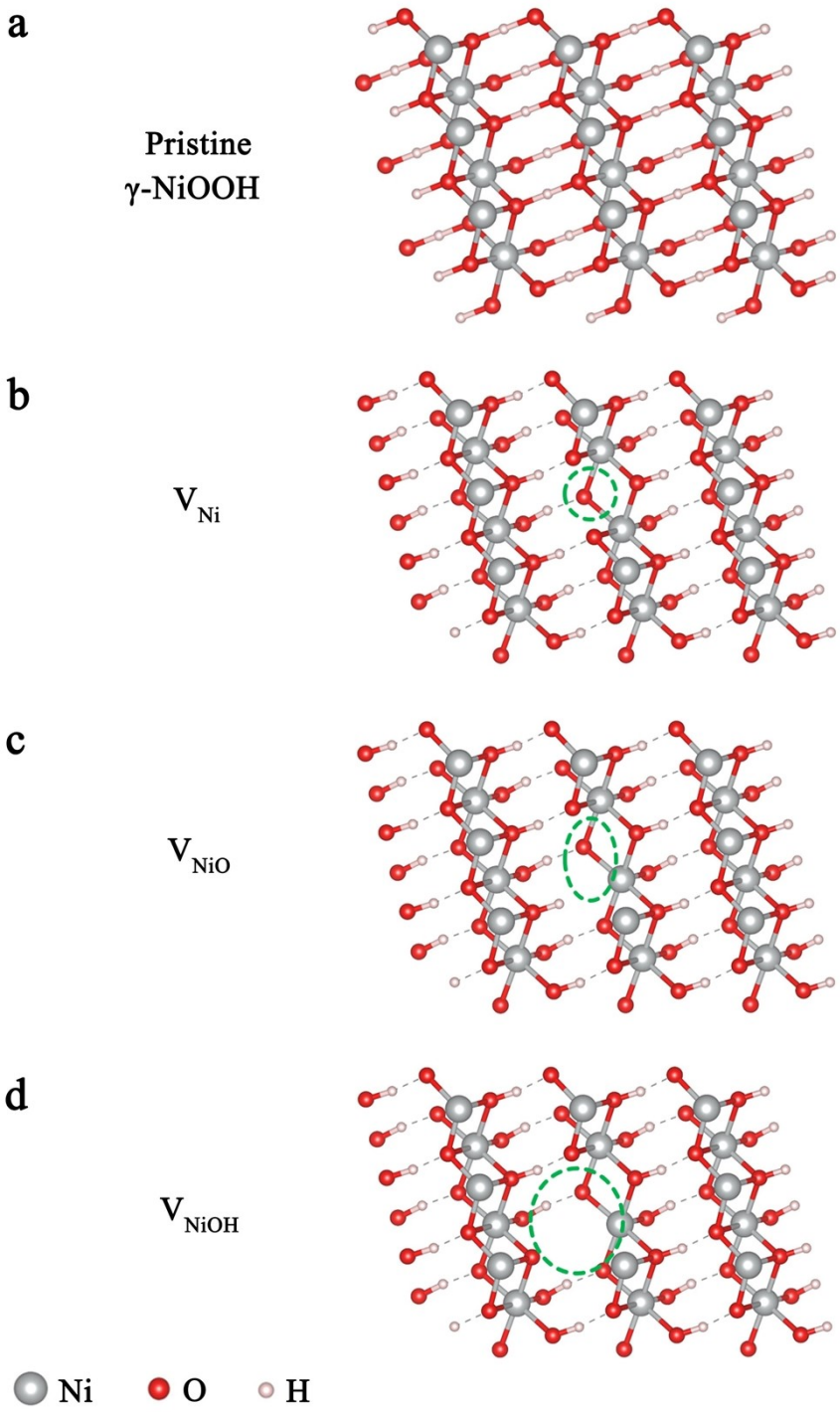

Figure S17. Top views of optimized geometries of pristine NiOOH, V_{Ni} (NiOOH with Ni cation vacancy), V_{NiO} (NiOOH with NiO cation vacancy) and V_{NiOH} (NiOOH with NiOH cation vacancy).

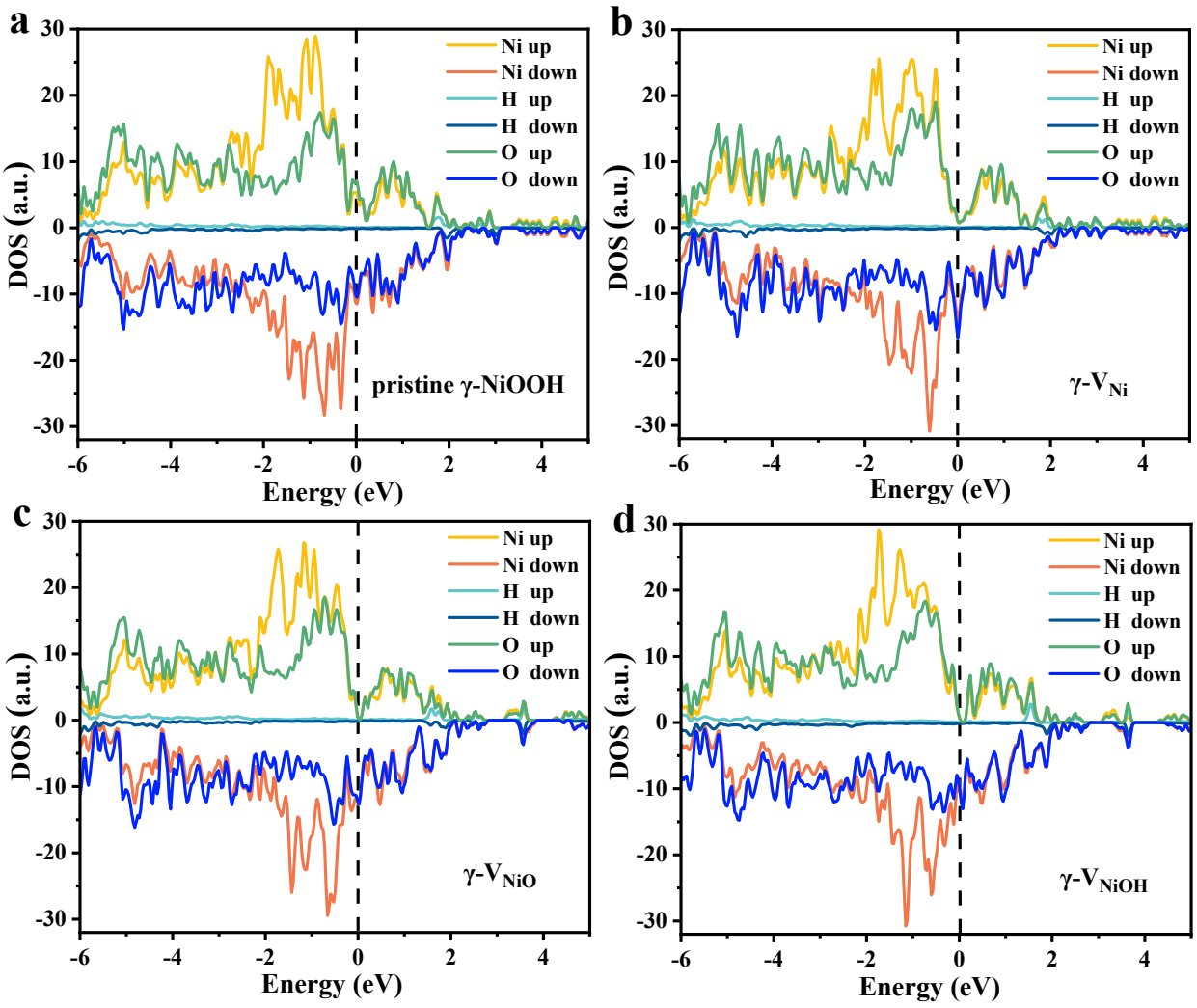

Figure S18. The corresponding DOS of (a) pristine γ-NiOOH, (b) γ-V_{Ni}, (c) γ-V_{NiO} and (d) γ-V_{NiOH}.

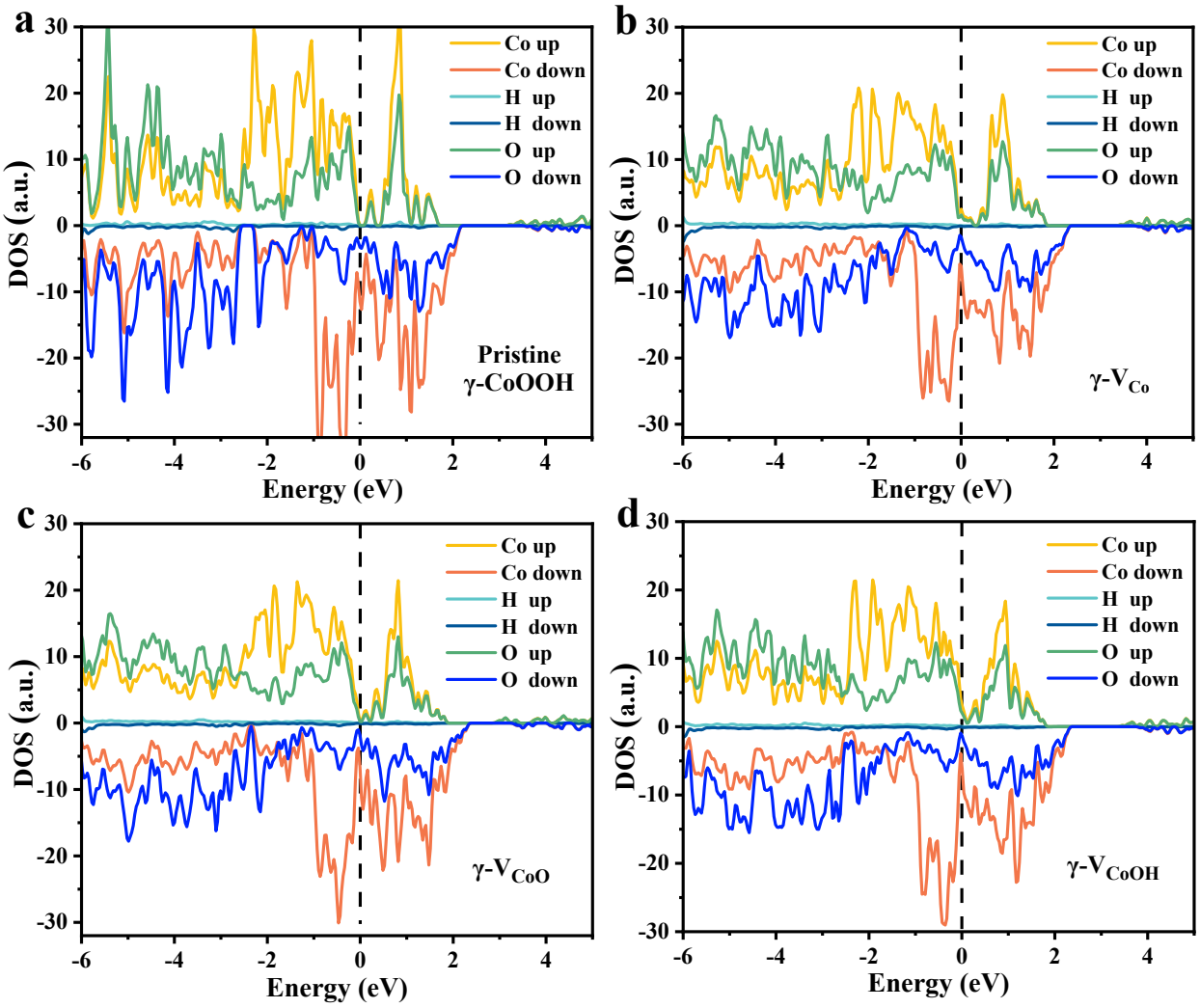

Figure S19. The corresponding DOS of (a) pristine γ-CoOOH, (b) γ-V_{Co}, (c) γ-V_{CoO} and (d) γ-V_{CoOH}.

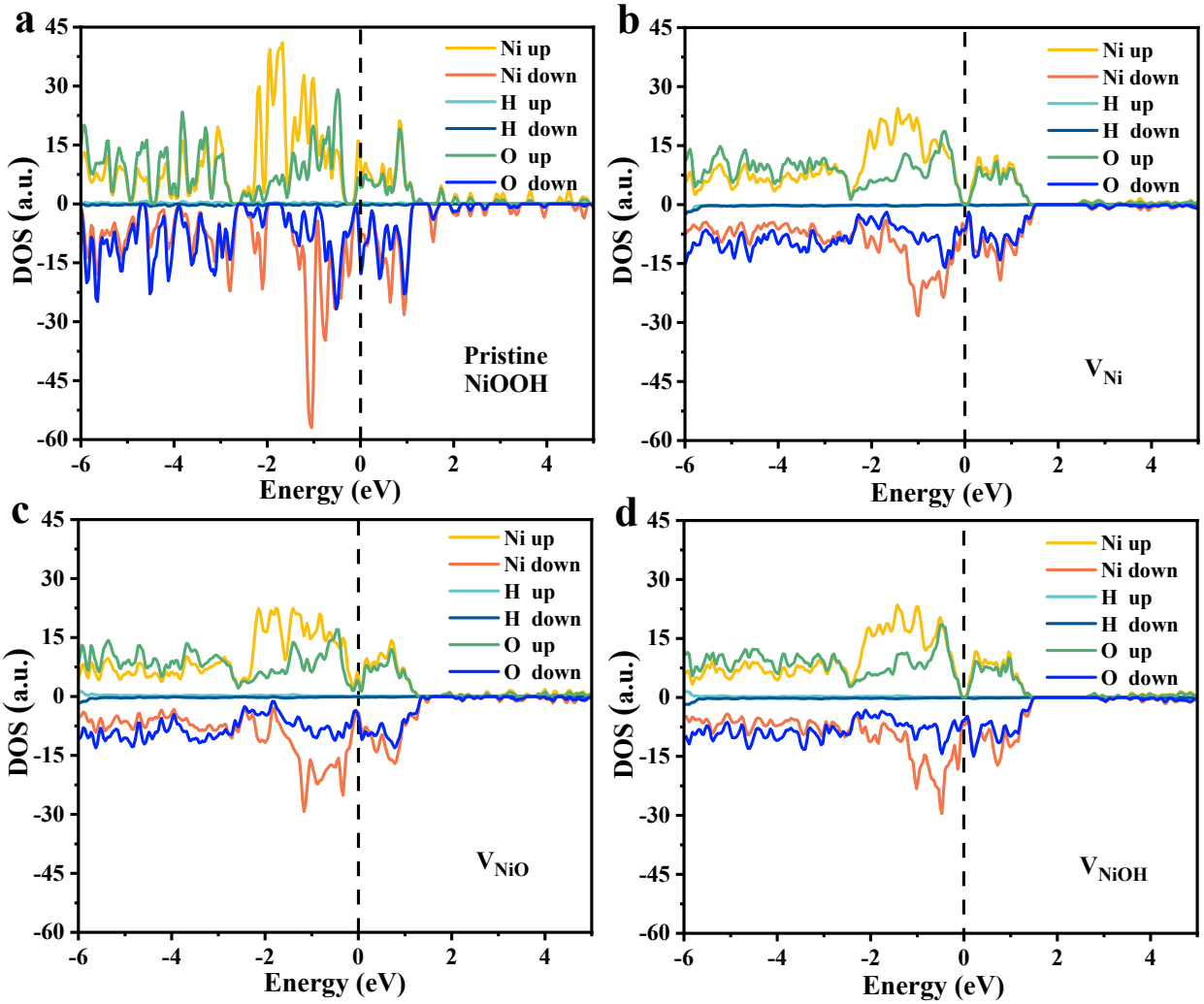

Figure S20. The corresponding DOS of (a) pristine NiOOH, (b) V_{Ni}, (c) V_{NiO} and (d) V_{NiOH}.

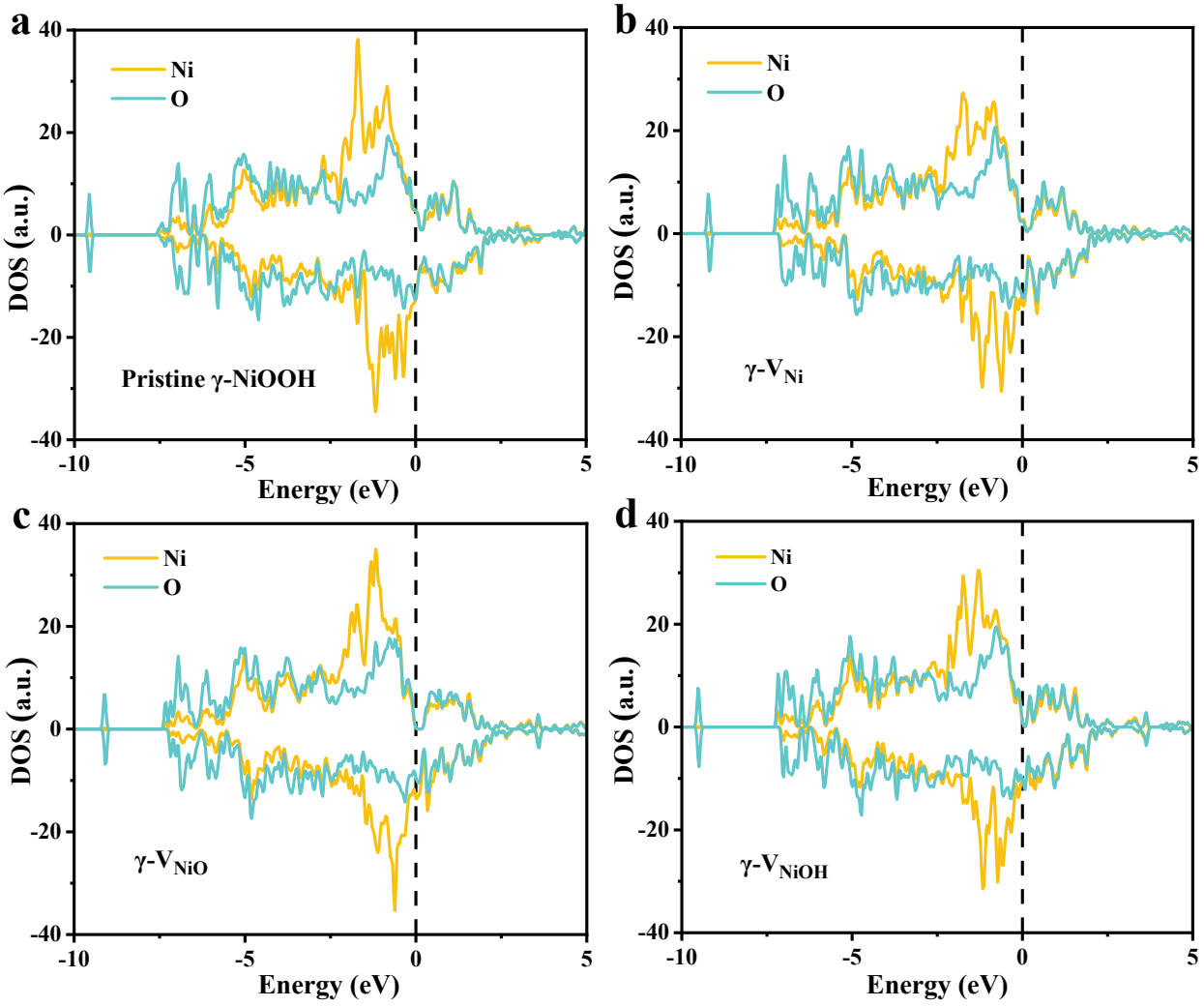

Figure S21. The corresponding DOS after the H_2O adsorption reaction on the corresponding adsorption site Ni and O in water molecules of (a) pristine γ-NiOOH, (b) γ-V_{Ni}, (c) γ-V_{NiO} and (d) γ-V_{NiOH}.

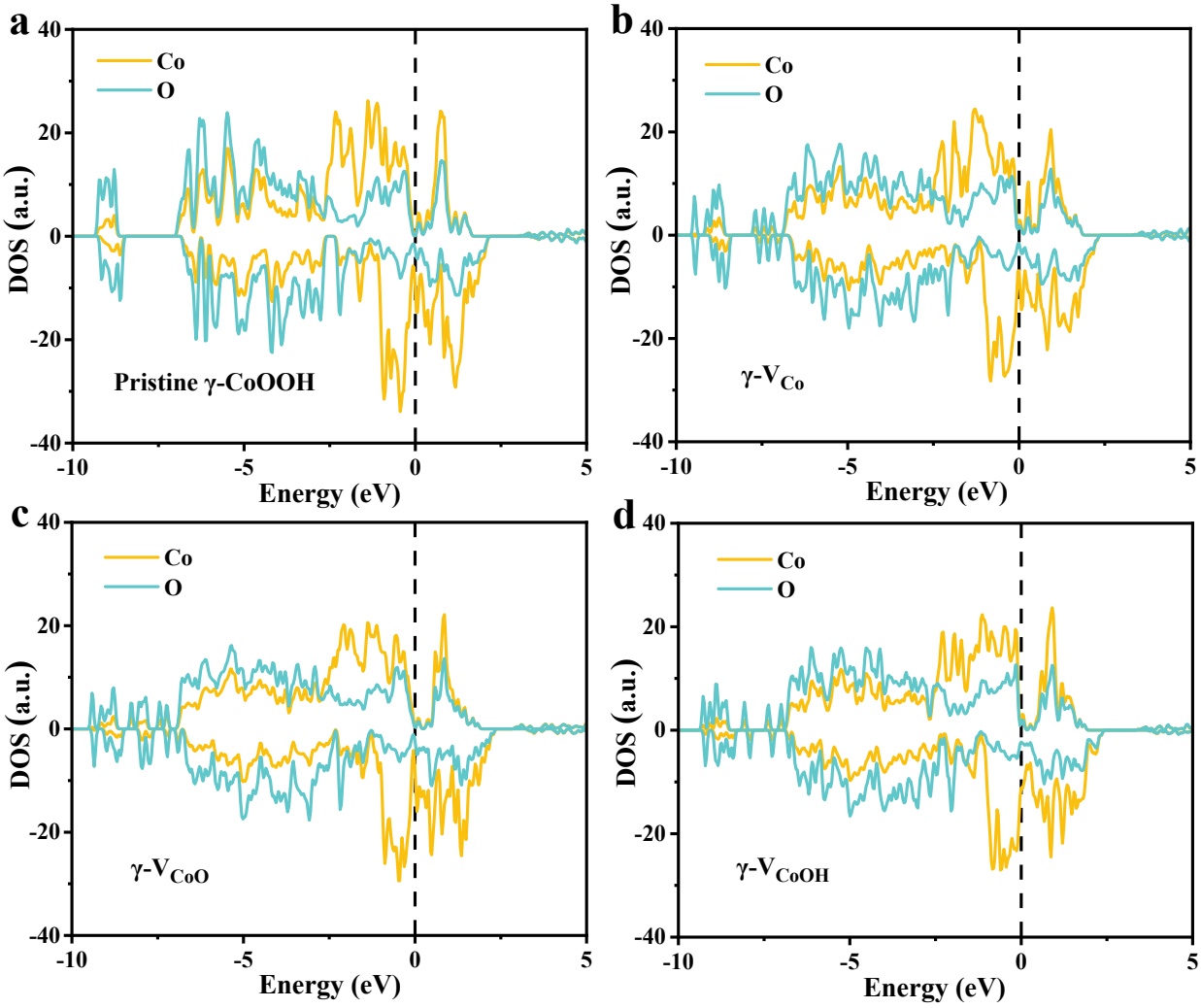

Figure S22. The corresponding DOS after the H_2O adsorption reaction on the corresponding adsorption site Co and O in water molecules of (a) pristine γ-CoOOH, (b) γ-V_{Co}, (c) γ-V_{CoO} and (d) γ-V_{CoOH}.

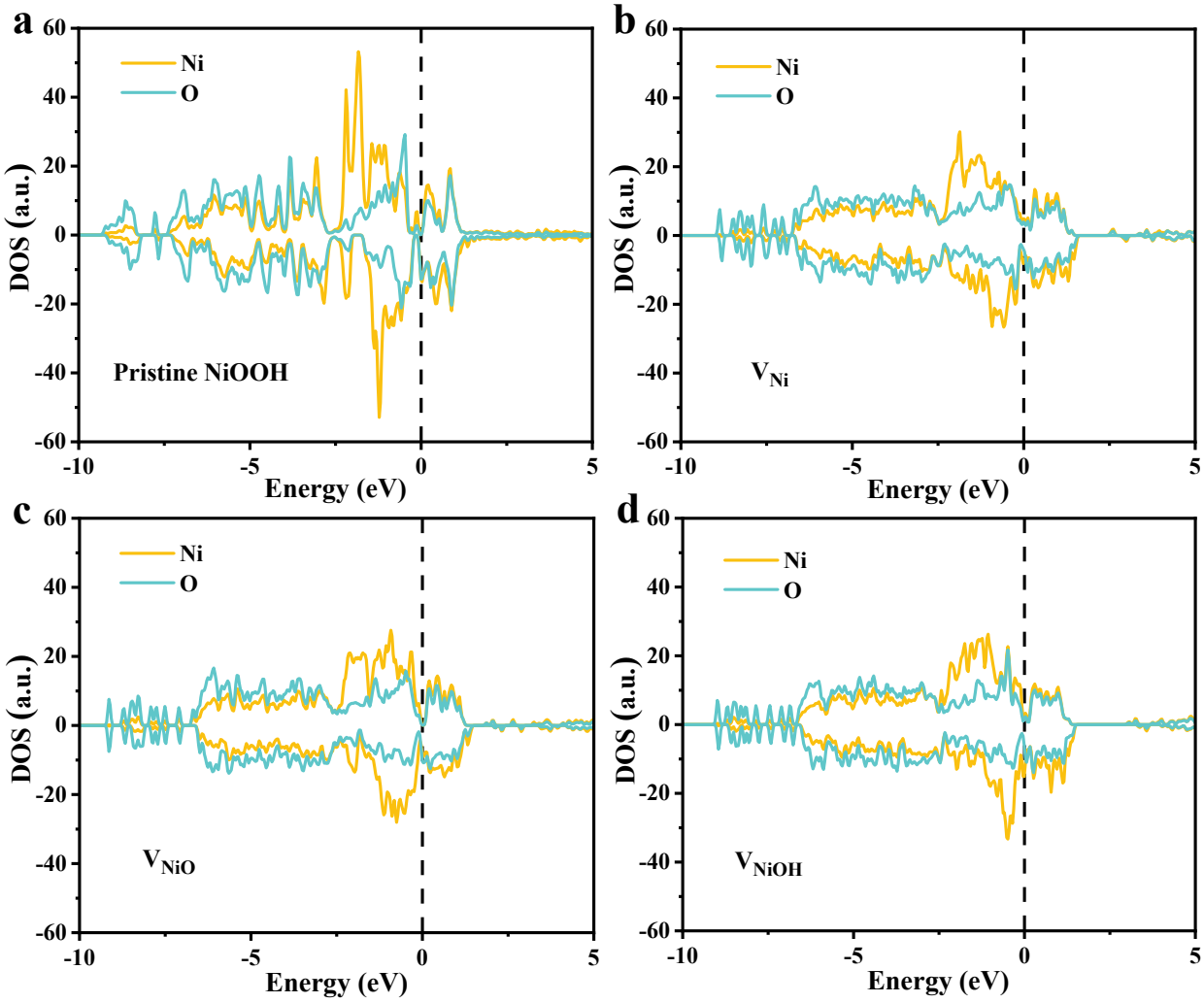

Figure S23. The corresponding DOS after the H_2O adsorption reaction on the corresponding adsorption site Ni and O in water molecules of (a) pristine NiOOH, (b) V_{Ni}, (c) V_{NiO} and (d) V_{NiOH}.

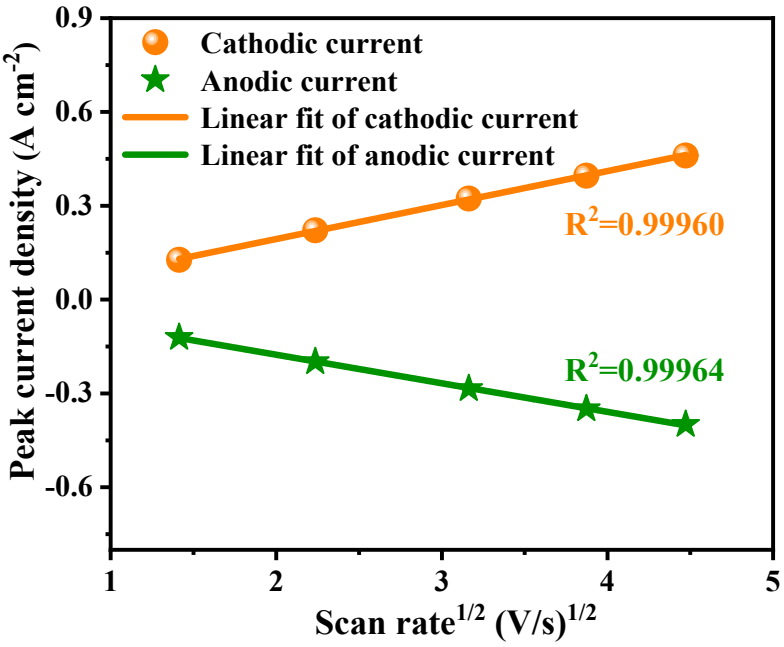

Figure S24. The corresponding function of peak current and the square of scan rates for Ni-Co oxyhydroxides.

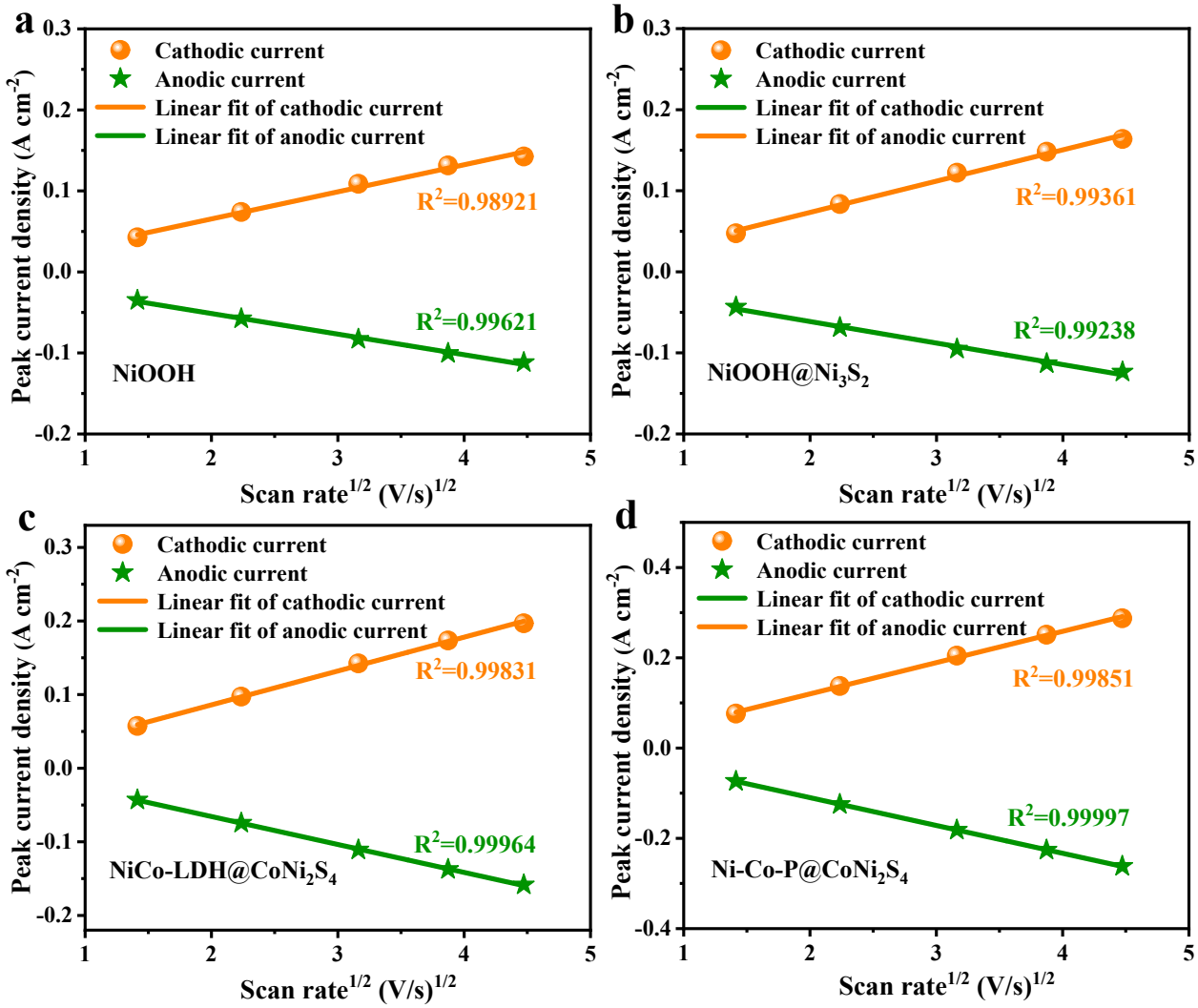

Figure S25. The corresponding function of peak current and the square of scan rates for (a) NiOOH, (b) $NiOOH@Ni_3S_2$, (c) $NiCo\text{-}LDH@CoNi_2S_4$ and (d) $Ni\text{-}Co\text{-}P@CoNi_2S_4$.

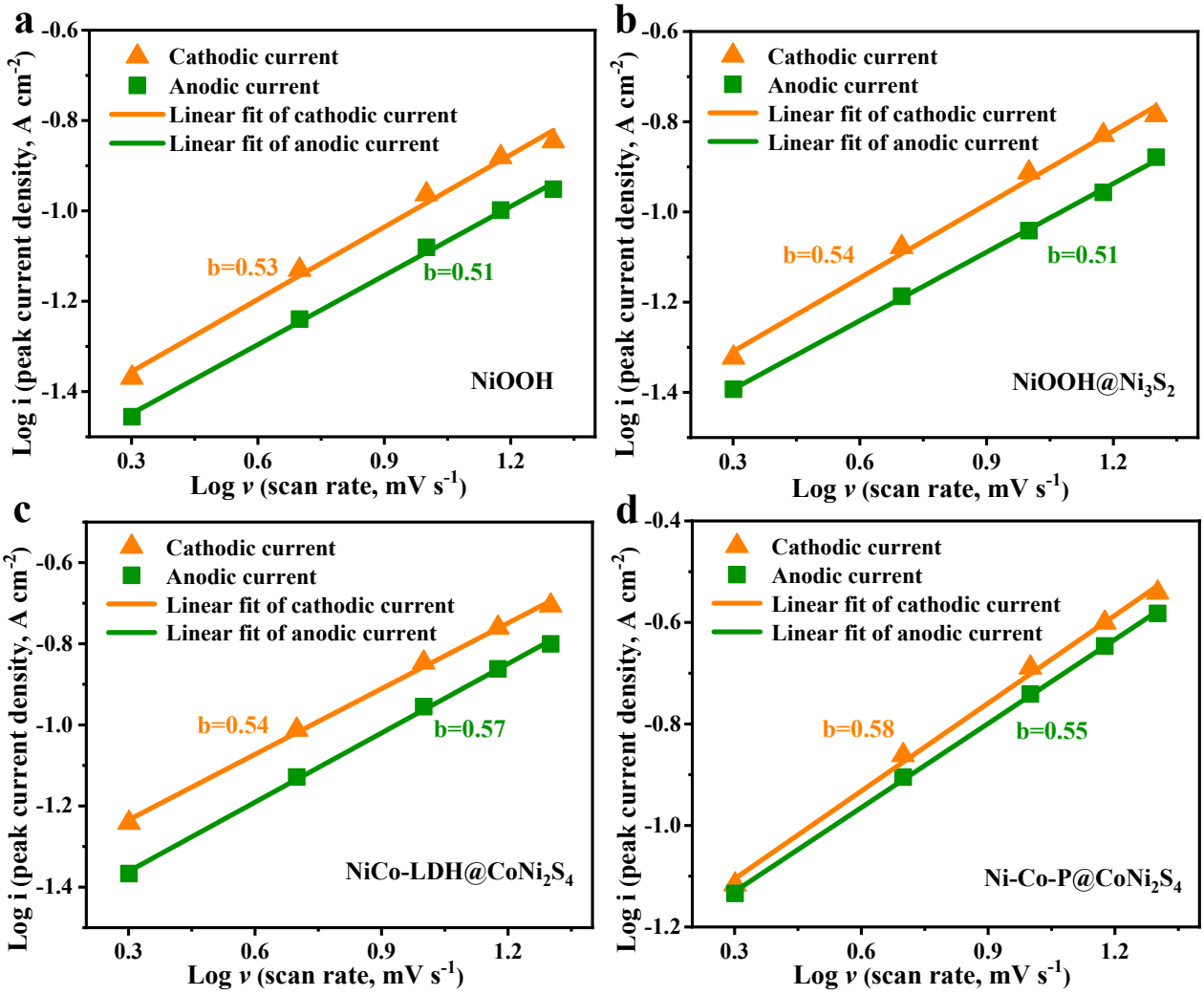

Figure S26. Relationship between the logarithm of scan rate and peak current of (a) NiOOH, (b) NiOOH@Ni_3S_2, (c) NiCo-LDH@$CoNi_2S_4$ and (d) Ni-Co-P@$CoNi_2S_4$.

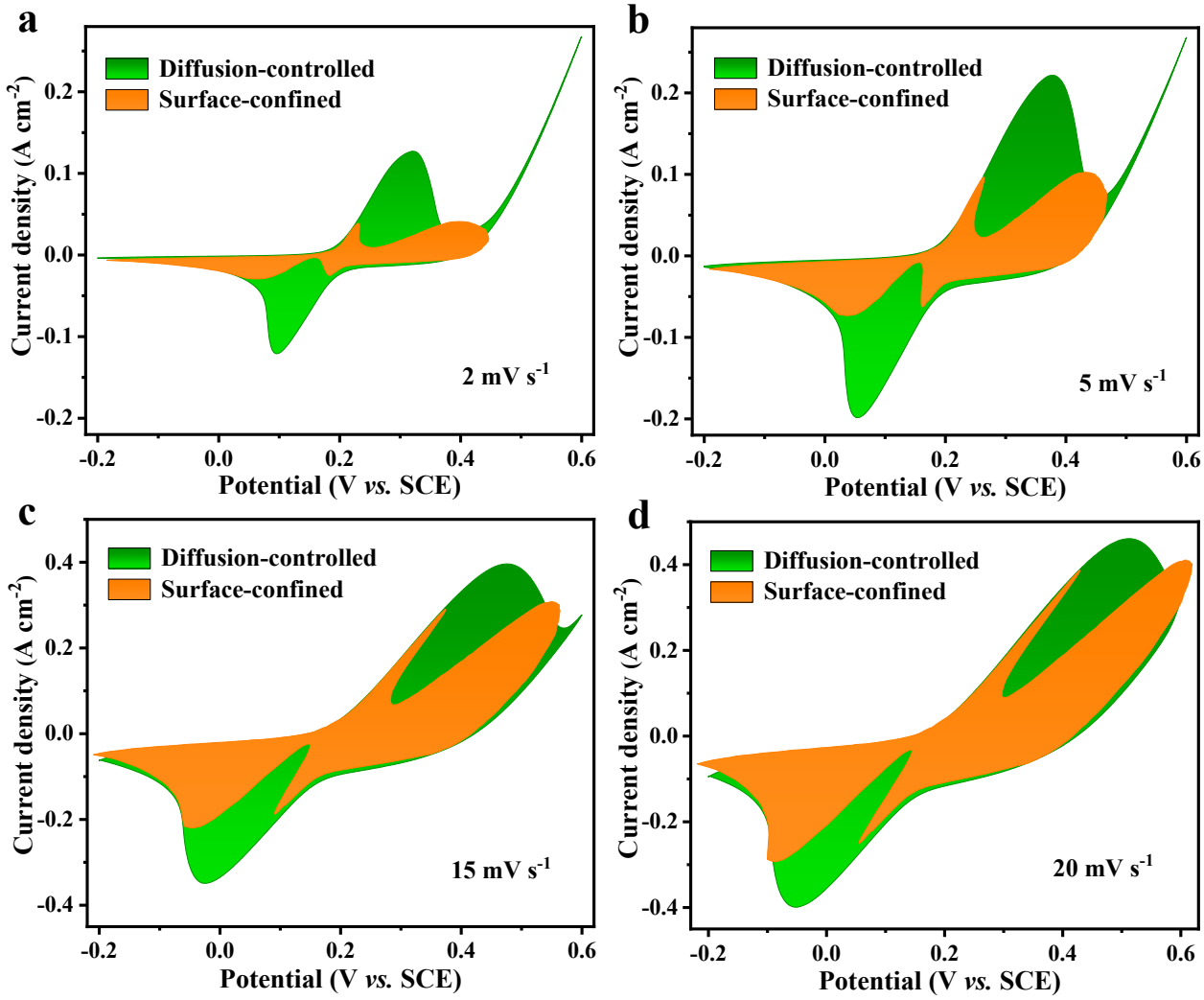

Figure S27. Surface-confined and diffusion-controlled contribution to charge storage of Ni-Co oxyhydroxides at (a) 2 mV s^{-1}, (b) 5 mV s^{-1}, (c) 15 mV s^{-1} and (d) 20 mV s^{-1}.

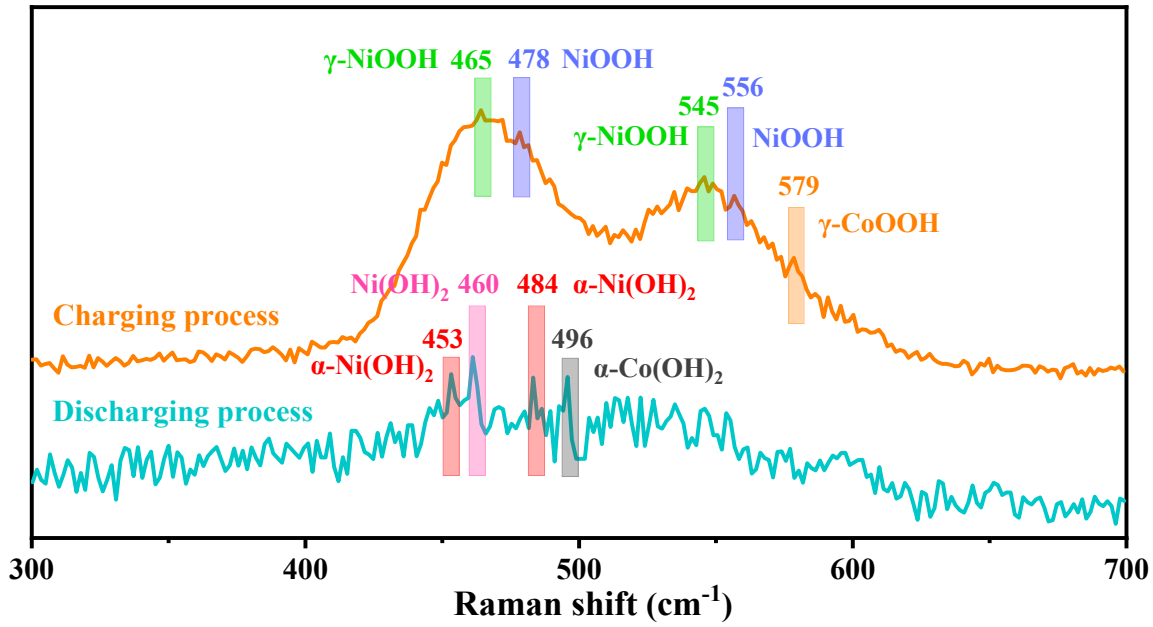

Figure S28. *In situ* Raman spectroscopy measurements of Ni-Co oxyhydroxides from charging process to discharging process.

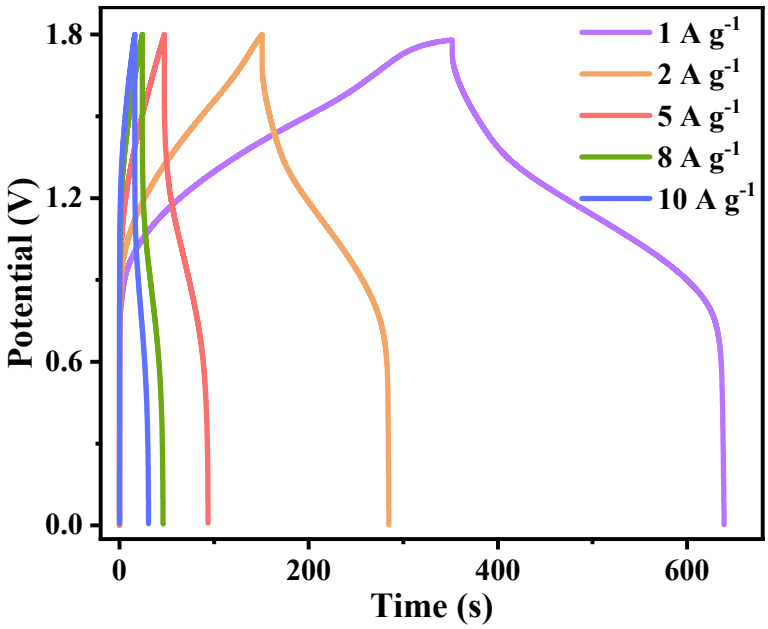

Figure S29. GCD curves of Ni-Co oxyhydroxides//AC all-solid-state ASC from 1 to 10 A g^{-1}.

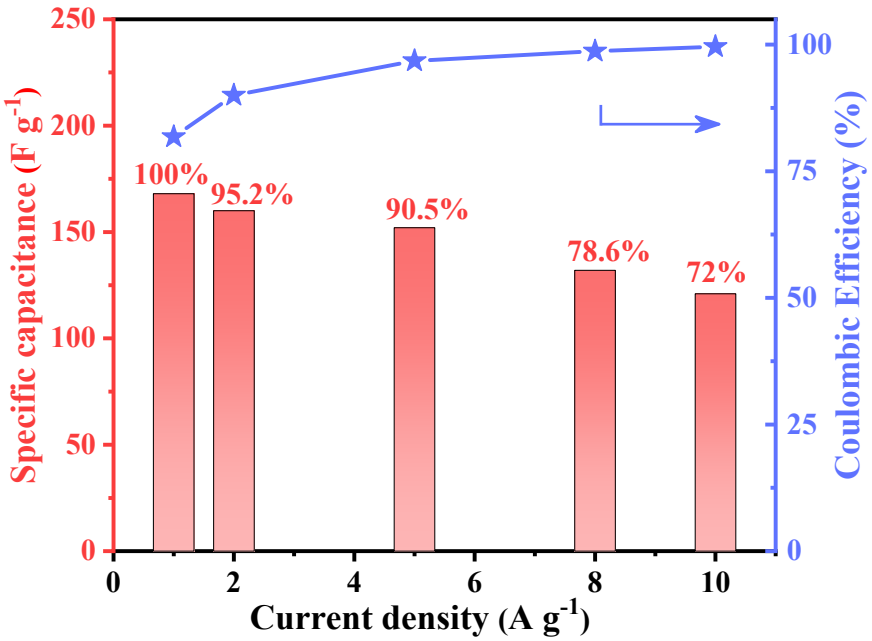

Figure S30. The specific capacitance and coulombic efficiency of Ni-Co oxyhydroxides//AC all-solid-state ASC at various current densities.

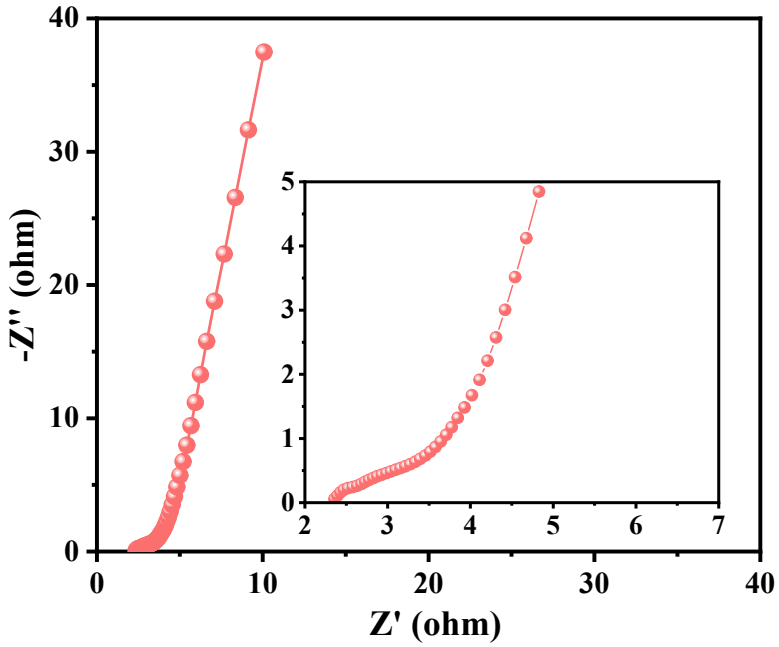

Figure S31. Nyquist plot of Ni-Co oxyhydroxides//AC all-solid-state ASC.

References

[1] M. Xie, M. Zhou, Y. Zhang, C. Du, J. Chen, L. Wan, *J. Colloid Interf. Sci.*, 2022, **608**, 79-89.

[2] W. He, C. Wang, H. Li, X. Deng, X. Xu, T. Zhai, *Adv. Energy Mater.*, 2017, **7**, 1700983.

[3] C. Wu, Z. Zhang, Z. Chen, Z. Jiang, H. Li, H. Cao, Y. Liu, Y. Zhu, Z. Fang, X. Yu, *Nano Res.*, 2021, **14**, 953-960.